Chemical Engineering Science 84 (2012) 155–169

Contents lists available at SciVerse ScienceDirect

Chemical Engineering Science

journal homepage: www.elsevier.com/locate/ces

Three-dimensional effects in laminar flow past a confined cylinder

V.M. Ribeiro [a], P.M. Coelho [b], F.T. Pinho [b], M.A. Alves [a,*]

[a] Departamento de Engenharia Química, CEFT, Faculdade de Engenharia da Universidade do Porto, Rua Dr. Roberto Frias, 4200-465 Porto, Portugal
[b] Departamento de Engenharia Mecânica, CEFT, Faculdade de Engenharia da Universidade do Porto, Rua Dr. Roberto Frias, 4200-465 Porto, Portugal

HIGHLIGHTS

- The laminar flow past a confined circular cylinder is investigated.
- The 3D nature of the flow is assessed for a wide range of cylinder aspect ratios.
- Flow visualizations and PIV measurements are presented.
- Numerical simulations agree with experimental measurements

ARTICLE INFO

Article history:
Received 23 March 2012
Received in revised form
25 July 2012
Accepted 2 August 2012
Available online 13 August 2012

Keywords:
Laminar flow
Computational fluid dynamics
Visualization
Confined cylinder flow
Low Reynolds number flow
PIV

ABSTRACT

An experimental and numerical study on the Newtonian fluid flow around a confined cylinder placed in a rectangular duct was undertaken in order to assess three-dimensional effects on the flow patterns. The cylinder was placed at the mid-plane to define a symmetric geometry with a 50% blockage ratio (*BR*, ratio between the cylinder diameter and the thickness of rectangular section). The flow visualizations by streak photography and the velocity measurements by particle image velocimetry were carried out for three different aspect ratios (*AR*, ratio between the length and diameter of the cylinder) of 16, 8 and 2 and the Reynolds number varied between creeping flow conditions ($Re \rightarrow 0$) up to the onset of time-dependent flow. The numerical calculations were performed in 3D meshes using an in-house finite volume code. They showed good agreement with experimental measurements and were also used to investigate the flow at very small and very large *AR*. For large values of *AR*, the results show unexpected velocity peaks near the cylinder end walls downstream of the cylinder for both inertia and diffusion controlled flow conditions. Increasing the aspect ratio of the cylinder does not reduce this local three-dimensional flow effect, which is found to occur near the ends of the cylinder at about one cylinder radius distance from the duct end walls. In contrast, reducing *AR* eliminated flow separation as expected for the Hele–Shaw type flows.

1. Introduction

Flows of Newtonian and non-Newtonian fluids around a confined circular cylinder are of relevance in a variety of industrial applications, the most typical case being the flow in heat exchangers, but including also other flows in food processing, flow through some porous media or in textile coating processes (Nishimura, 1986). The ubiquity of cylinder flow in addition to the absence of geometrical singularities and the specificities of some of its flow characteristics, especially for viscoelastic fluids, made it an established benchmark in the development of numerical methods for very low Reynolds number flows of non-Newtonian fluids (Brown and McKinley, 1994).

The flow around a finite length cylinder leads to three-dimensional (3D) effects, which are disregarded in traditional studies using two-dimensional (2D) geometries (Verhelst and Nieuwstadt, 2004); this is achieved experimentally by using long cylinders often with the help of end-plates. The impact of 3D effects on the overall flow characteristics depends essentially on the aspect ratio of the cylinder and the Reynolds number, but is also determined by the type of confinement and the rheology of the working fluid.

Before proceeding with a review of the state of the art, we note that throughout the literature the Reynolds number is defined both using the cylinder diameter, Re_D (Nieuwstadt and Keller, 1973; Williamson, 1996a,b; Leweke and Williamson, 1998; Coelho and Pinho, 2003; Chakraborty et al., 2004) and the cylinder radius, *Re* (Thom, 1933; Kawaguti, 1953; Thompson et al., 1996; Verhelst

* Corresponding author. Tel.: +351 225081680; fax: +351 225081449.
E-mail addresses: vera@fe.up.pt (V.M. Ribeiro), pmc@fe.up.pt (P.M. Coelho), fpinho@fe.up.pt (F.T. Pinho), mmalves@fe.up.pt (M.A. Alves).

0009-2509/$ - see front matter © 2012 Elsevier Ltd. All rights reserved.
http://dx.doi.org/10.1016/j.ces.2012.08.003

and Nieuwstadt, 2004; Ferreira, 2006) as characteristic length scale. In this work the cylinder radius will be used in the definition of the Reynolds number, but in this section both definitions will be referred to.

Studies of Newtonian fluid flow around a cylinder started a long time ago, with important early contributions by Strouhal (1878), Hiemenz (1911), and von Kármán (1911). Comprehensive reviews on the state of the art were written by Cantwell and Coles (1983), Telionis et al. (1992), Williamson (1996b) and Zdravkovich (1997). Most of the studies concerning Newtonian fluid flow around a cylinder focus on the vortex shedding phenomenon, the effect of blockage ratio (BR, defined as the ratio between the cylinder diameter and the thickness, H, of the rectangular section), the effect of aspect ratio (AR, defined as the ratio between the length and diameter of the cylinder) and the dynamics in various flow regimes (Sumer and Fredsoe, 1997). These investigations are limited in scope given the breadth of possibilities: they usually either concern flow at Reynolds numbers (Re) below the critical value for the onset of vortex shedding ($Re < Re_{(vs)}$) or above this condition ($Re > Re_{(vs)}$), unbounded ($BR \approx 0$) or bounded flow and two-dimensional or three-dimensional flow.

Two-dimensional flows require cylinders of large AR, or at least intermediate values of AR with the observation being made far from the side walls. Flows under these conditions have been extensively studied and more than 40 years ago Gerrard (1966) proposed a mechanism to explain vortex shedding based on the formation and diffusion lengths, whereas Williamson (1996b) reviewed extensively the vortex dynamics in the cylinder wake and provided the main flow characteristics within each flow regime. More recently, the experiments of Coelho and Pinho (2003) on non-Newtonian fluid flows around cylinders with $AR=6$ and 12 proceeded to the identification and demarcation of flow regimes for some viscoelastic fluids at $50 \leq Re_D \leq 9000$.

From the earlier studies, for 2D flow past an unbounded circular cylinder (i.e. $BR \approx 0$), the critical Reynolds number for the onset of the flow separation number, $Re_{D(s)}$, varied between $3.2 < Re_{D(s)} < 7$ (Sen et al., 2009). Sen et al. (2009) concluded that the critical value for the onset of flow separation is $Re_{D(s)} \approx 6.29$ for $BR=0.005$, i.e., for what is considered essentially an unbounded flow. The critical Reynolds number for the onset of laminar vortex shedding is $Re_{(vs)} \approx 23.5$ for aspect ratios above 45 (Lee and Budwig, 1991; Williamson, 1996b; Sahin and Owens, 2004). For aspect ratios below 45, the critical Reynolds number for the onset of vortex shedding increases, as the value of aspect ratio decreases (Nishioka and Sato, 1974). According to Lee and Budwig (1991), for $BR \approx 0$ and $AR=16$, 8 and 2, i.e., for the values of aspect ratio under study in this work, the critical Reynolds numbers for the onset of laminar vortex shedding are $Re_{(vs)} \approx 30$, $Re_{(vs)} \approx 40$ and $Re_{(vs)} \geq 70$, respectively.

According to Payne (1958), early numerical calculations of the steady flow past a confined cylinder at $Re \approx 10$ and 20 were presented by Thom (1933), at $Re_D \approx 40$ by Kawaguti (1953) and at $1 \leq Re_D \leq 40$ by Nieuwstadt and Keller (1973). More recently, Zdravkovich (2003) established a generic classification of the blockage effects. For $BR < 0.1$ the blockage effect is small and may be neglected; for $0.1 < BR < 0.6$ the blockage effect modifies the flow; for $BR > 0.6$ the flow is radically influenced by the blockage effect. Sen et al. (2009) investigated the effect of blockage ratio, in the range $0.000125 \leq BR \leq 0.8$ for $6 < Re_D < 40$, and concluded that the bubble length, separation angle and the critical Reynolds number for the onset of the flow separation $Re_{(s)}$, exhibit non-monotonic variations with blockage ratio and that this effect is insignificant for $BR \leq 0.01$. The numerical study of the Newtonian fluid flow past a circular cylinder confined in a rectangular channel of Chakraborty et al. (2004) explored the interplay of flow parameters such as the length of the recirculation, the drag coefficient and the angle of flow separation in the range $Re_D \approx 0.1$–200. Sahin and Owens (2004) investigated numerically the effect of blockage ratio on the linear stability of confined cylinder flow and reported on the neutral curve and stability maps, but their analysis is restricted to 2D flow. The effect of the blockage ratio in the 2D flow past a cylinder in a channel was also investigated numerically by Rao et al. (2011), using Newtonian fluids and non-Newtonian fluids described by the power-law model, for the range of vortex shedding, $40 \leq Re \leq 140$.

Three-dimensional effects in the Newtonian circular cylinder flows at $Re \geq Re_{(vs)}$ were also extensively investigated. Gerich and Eckelmann (1982) looked at the effect of end-plates on the shedding frequency and Norberg (1994) studied experimentally the influence of aspect ratio at low blockage ratio in the range of Re_D from 50 up to 4×10^4. Thompson et al. (1996) predicted numerically two shedding modes for different Re and the existence of the two modes for $Re \approx 250$. Williamson (1996a) and Leweke and Williamson (1998) explained the origin of the instabilities leading to the two modes of 3D vortex shedding in the wake transition regime, i.e., for Re_D from 190 to 240. The study of 3D effects and of the influence of aspect ratio on the characteristics of laminar flow around a confined cylinder at $Re \leq Re_{(vs)}$ has been carried out recently by Ferreira (2006), who considered the range $0 \leq Re \leq 40$ and also concluded that the Reynolds number marking the appearance of a steady separated flow in the rear region is $Re_{(s)} \approx 6$.

Since the establishment of the 2D creeping flow past a circular cylinder as a benchmark test case for non-Newtonian fluids there was an increased need to understand well the corresponding Newtonian fluid flows and consequently a variety of experimental and numerical studies for the flow around a confined cylinder at $Re \leq Re_{(vs)}$ were carried out. The experimental studies of Verhelst and Nieuwstadt (2004) for the Newtonian and non-Newtonian fluids flowing past a confined cylinder in a rectangular channel with a blockage ratio of 50% and aspect ratio of 16 showed the appearance of 3D effects near the end walls, but these were not described in detail. In a numerical investigation of laminar Newtonian and non-Newtonian flows around confined cylinders, Ferreira (2006) found the appearance of velocity peaks near the end walls in the range of $2 \leq AR \leq 16$ and $Re \leq 40$, but these predictions lacked experimental confirmation and an in depth analysis of the 3D effects, so it is not yet clearly established when the low Reynolds number flow around a cylinder can be considered to be essentially 2D and what are the flow characteristics when the flow is markedly 3D.

Our long term objective is to investigate 3D flows of non-Newtonian fluids with viscoelastic behaviour, but an extensive investigation of this nature is necessarily long and expensive, because of the wide range of possible fluid properties and types. For a purely numerical investigation, the non-linear nature of the viscoelastic fluids also requires large computational resources. In any case, such endeavour must necessarily start with the investigation of the corresponding Newtonian fluid dynamics in detail and given the lack of information identified above, that is precisely the purpose of the present contribution. In this work, this is achieved both numerically and experimentally and we provide an extensive set of reference cases against which the results of the non-Newtonian fluids can be compared with in the future. Specifically, this is achieved experimentally by considering the Newtonian fluid flow across a single confined cylinder with a blockage ratio of 50% (the typical benchmark case in computational rheology) as a function of the Reynolds number and of the aspect ratio, which is varied between 2 and 16 (specifically for $AR=16$, 8 and 2), under steady flow conditions (i.e. for $Re \leq Re_{(vs)}$),

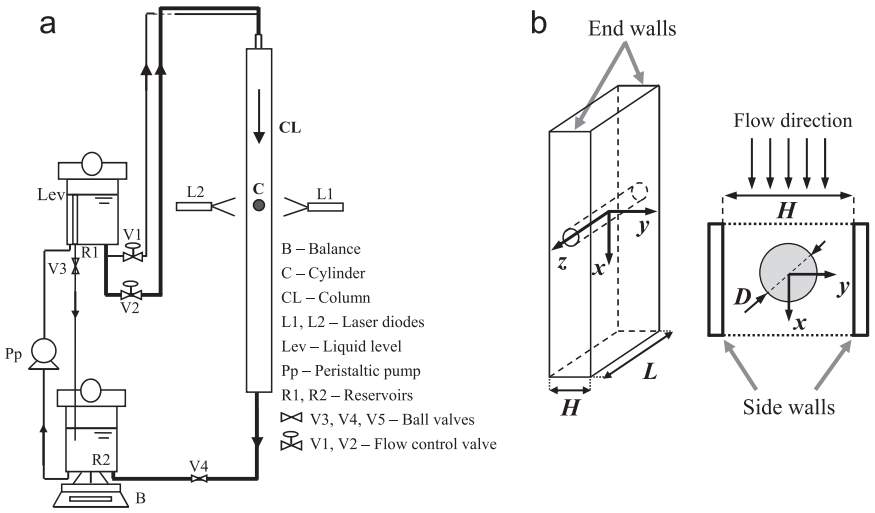

Fig. 1. (a) Experimental set-up and (b) test section and the coordinate system.

except for a few illustrative cases above $Re_{(vs)}$. All the experimental cases are numerically simulated and additionally computational results are also presented for other values of AR to better assess the influence of this geometrical parameter. According to the literature, for $AR=16$ and BR of 50% the Reynolds number marking the appearance of a steady separated flow in the rear region is $Re_{(s)} \approx 6$ (Ferreira, 2006), whereas the Reynolds number for the onset of time-dependent vortex shedding is $Re_{(vs)} \approx 40$ for the limiting case of large AR (i.e. 2D flow) (Sahin and Owens, 2004; Ferreira, 2006); accordingly, the present study considers primarily this range of Re.

The remainder of this paper is organized as follows: the experimental set-up and techniques are described in Section 2 and Section 3 presents the fluid characterization. The governing equations and a brief outline of the numerical method are described in Section 4. Section 5 presents and discusses the experimental results and compares them with the numerical simulations. Section 6 summarizes the main conclusions of this work.

2. Experiments

2.1. Experimental set-up

The experimental set-up is a closed system shown in Fig. 1a. The test section represented in Fig. 1b is a 1700 mm long duct with a rectangular cross section with a thickness (H) of 20 mm and a variable width (L), where the confined cylinder with 10 mm diameter (and length L) is located. The cylinder is located 630 mm downstream of the duct inlet and is positioned at the mid plane to define a symmetric geometry with a 50% area blockage ($BR=D/H$).

As illustrated in Fig. 1a, the fluid flows through the rectangular duct by gravity (from reservoir R1 to reservoir R2) and a variable speed peristaltic pump (Pp) (ref. Lav 400 l/h, Dosim) recirculates the fluid back to the constant head reservoir R1, in order to maintain a constant liquid level (Lev) at the upper reservoir with the help of the overflow discharge pipe fitted with valve V3 (normally fully opened). The pump is switched off to measure the flow rate using a digital balance (KERN DS 36 k0.5; readout of 0.5 g; maximum range of 36 kg) which is placed under reservoir R2 (during the measurement the liquid level variation in reservoir R1 is small). This balance is monitored by LabView v7.1 software to record time and weight of fluid. The flow rate in the test section is controlled by changing the vertical position of reservoir R1 using an electric winch (not illustrated in Fig. 1a) and through proper regulation of valves V1 and V2, with V1 being used for low flow rates and V2 for higher flow rates. The tubes connecting valves V1 and V2 to the test section have different diameters, which are selected according to the range of flow rates required.

Table 1
Aspect ratios under study.

	$AR=16$	$AR=8$	$AR=2$
L (mm)	160.0	80.0	20.0
D (mm)	10.0	10.0	10.0

The origin of the coordinate system represented in Fig. 1b is located at the centre of the cylinder, with the positive x-axis pointing in the streamwise downstream direction, the y-axis in the cross-stream direction (normal to the main rectangular duct walls) and the z-axis in the spanwise direction (along the cylinder axis).

One of the end walls can be moved along the spanwise direction (z) in order to change the width (L), and consequently the aspect ratio ($AR=L/D$) of the geometry. Three different aspect ratios ($AR=16$, 8 and 2) were used in the experiments with the corresponding dimensions of the rectangular duct described in Table 1. Spacers were also used to ensure that the duct dimensions were kept constant along the test section.

The duct inlet has a distributor with a maximum of six injectors in order to obtain a velocity profile as uniform as possible at the inlet of the rectangular duct. The distance between the distributor and cylinder under study allows achieving a fully-developed velocity profile well upstream of the cylinder; the exit of the duct is also sufficiently far away not to affect the flow dynamics in the vicinity of the cylinder. Most of the experiments were carried out under steady flow conditions, except for some flow visualizations conducted at higher Re to observe the vortex shedding phenomenon.

2.2. Experimental techniques

Flow visualizations using long time exposure streak photography and detailed velocity measurements using Particle Image Velocimetry (PIV) were carried out to characterize the flow field. Both techniques were used at various xy planes and in addition PIV measurements were taken at the symmetry plane $y/R=0$.

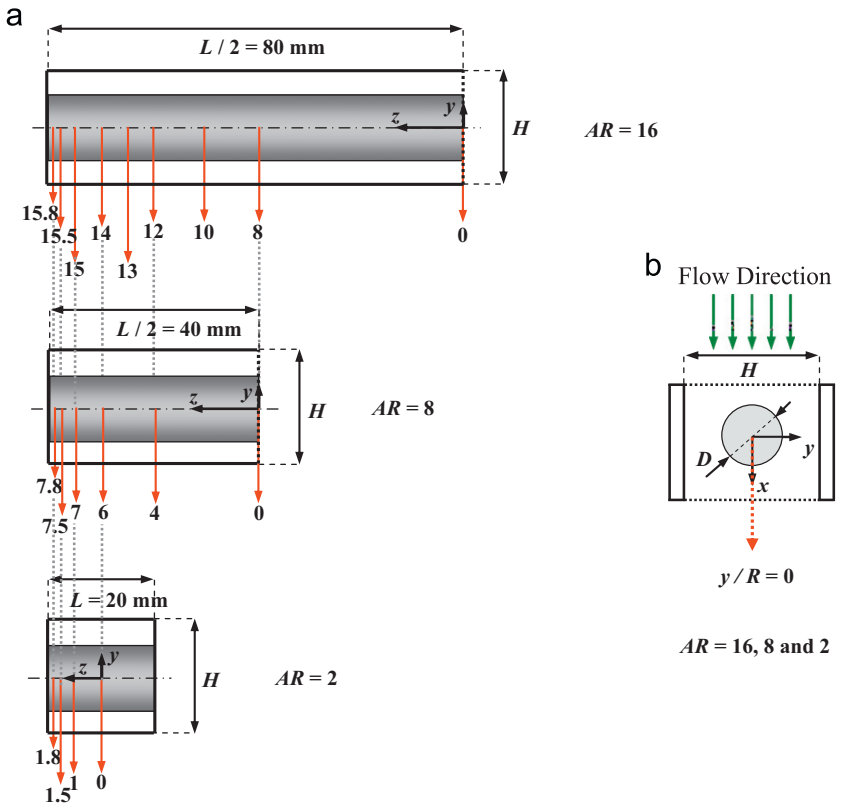

Fig. 2. Planes under study for $AR=16$, $AR=8$ and $AR=2$: (a) along the cylinder at different values of $|z/R|$ and (b) symmetry plane, $y/R=0$.

Fig. 2 shows the planes where measurements were carried out for each *AR*.

2.2.1. Flow visualization

In the study of flow patterns and recirculation length, using long time exposure streak photography, the flow was continuously illuminated using two co-planar 635 nm 5 mW laser diodes L1 and L2 (Vector, model 5200-20) equipped with cylindrical lenses to create a light sheet perpendicular to the cylinder axis (cf. Fig. 1a). The fluid contained a suspension of reflective tracer particles (hollow glass spheres with 10 μm diameter—HGS-10, Dantec Dynamics) at a weight concentration of 30 ppm. The reflected light was captured by a digital camera (CANON EOS 30D) equipped with a macro lens (EF100 mm, f2.8) placed perpendicularly to the laser light sheet to record the flow pathlines. The exposure time was varied depending on the flow rate, ranging between 1 s and 30 s. The two laser diodes and the digital camera moved simultaneously, to simplify the adjustments for each plane under study (cf. Fig. 2), using a manual traversing table with a relative positioning precision of ± 0.01 mm. The use of two laser diodes, instead of only one, minimized shadows around the cylinder.

2.2.2. Particle image velocimetry—PIV

The detailed measurements of velocity fields were carried out using a PIV system (Dantec Dynamics). The plane under investigation was illuminated by a double pulsed Nd:YAG laser (Solo PIV III, New Wave Research), which generates consecutive pairs of light sheets with a wavelength of 532 nm and a maximum energy of 50 mJ/pulse. The two consecutive pulses of light illuminated the suspended particles, which reflected light allowing the determination of the corresponding velocities from their displacement. The time between two consecutive pulses was short and was adjusted according to the flow conditions, and in particular to the average velocities being measured, and varied between 14 ms and 2.3 s. The images were acquired using a digital CCD camera (FlowSense 2M, Dantec Dynamics) coupled with a Nikon AF Micro lens of 60 mm focal length. At least 50 pairs of images were acquired for each flow rate and the velocity field was determined by ensemble-averaging the corresponding velocity maps. FlowManager v4.60 software was used to process each image pair using an adaptive-correlation algorithm, in order to generate a two-dimensional velocity vector map on interrogation windows of 32×32 pixels, with 50% overlap. The velocity field is validated using a moving average criterion and the process was carried out for all the double images recorded, resulting in an averaged velocity field.

3. Fluid characterization

All experiments were carried out with a Newtonian fluid, a 40% by weight aqueous solution of glycerine, which was seeded with tracer particles, as described in Section 2. The particle concentration satisfies the recommended criterion for PIV of having at least 5–10 particles per interrogation area (Adrian, 2005). In order to minimize bacteriological growth in the fluid and prevent its degradation, a biocide was added at a weight concentration of 25 ppm (Kathon LXE, Rohm and Haas).

To measure the dynamic viscosity of the Newtonian fluid at temperatures ranging from 288.2 K to 301.2 K a Physica MCR 301 shear rheometer was used with a 75 mm cone-plate system with 1° angle. The dependency of the dynamic viscosity (μ) on the absolute temperature (T) can be described by an Arrhenius equation in the form (Dealy and Plazek, 2009)

$$\ln\frac{\mu}{\mu_0} = \frac{\Delta H}{R}\left(\frac{1}{T}-\frac{1}{T_0}\right), \tag{1}$$

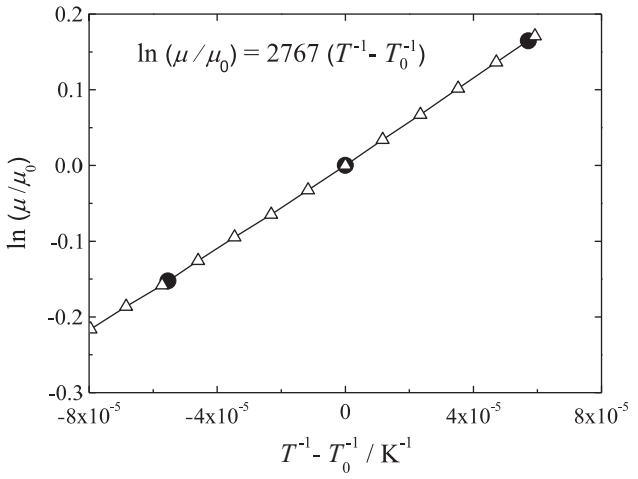

Fig. 3. Influence of temperature on the dynamic viscosity of the Newtonian fluid studied (Δ) and comparison with a 40 wt% glycerine aqueous solution (●) reported by Sheely (1932) (T_0=293.2 K).

where μ_0 represents the dynamic viscosity at reference absolute temperature T_0 (293.2 K), ΔH represents the activation energy for flow, and R is the universal gas constant.

The variation of dynamic viscosity with temperature is shown in Fig. 3 and it is clear that this variation is well described by the Arrhenius equation. The viscosity at the reference temperature, T_0=293.2 K, is 0.00376 Pa s and $\Delta H/R$=2767 K. The density of the solution, measured at 293.2 K using a pycnometer, was 1102 kg/m^3.

4. Governing equations and the numerical method

The governing equations describing the isothermal laminar flow of an incompressible fluid are the mass conservation equation,

$$\nabla\cdot\mathbf{u}=0, \tag{2}$$

and the momentum equation,

$$\rho\left(\frac{\partial\mathbf{u}}{\partial t}+\nabla\cdot\mathbf{uu}\right)=-\nabla p+\nabla\cdot\boldsymbol{\tau}, \tag{3}$$

where $\mathbf{u}$ represents the velocity vector, ρ the fluid density, t the time, p the pressure and $\boldsymbol{\tau}$ the extra-stress tensor. For the Newtonian fluids and through the application of Newton's law of viscosity, the extra-stress tensor can be written explicitly as

$$\boldsymbol{\tau}=\mu(\nabla\mathbf{u}+\nabla\mathbf{u}^{\mathrm{T}}) \tag{4}$$

The conservation of mass and the momentum equations were solved numerically using an in-house finite-volume code, which has been extensively verified (Oliveira et al., 1998, 2007, 2008b) and the implementation model validated against experimental data (Escudier et al., 2000; Oliveira et al., 2008a).

The numerical method is based on the time-marching version of the SIMPLEC pressure correction algorithm formulated for collocated variables (Oliveira et al., 1998). The continuity and momentum equations for the Cartesian velocity vector written in non-orthogonal coordinates are integrated in space over each of the computational cells of volume V_P, and in time over a time step Δt, to form sets of linearized algebraic equations. The discretization of the governing equations is based on central differences for diffusion terms and for the convective terms the interpolating scheme employed is the CUBISTA high-resolution scheme (Alves et al., 2003), formally of third-order accuracy in smooth fields.

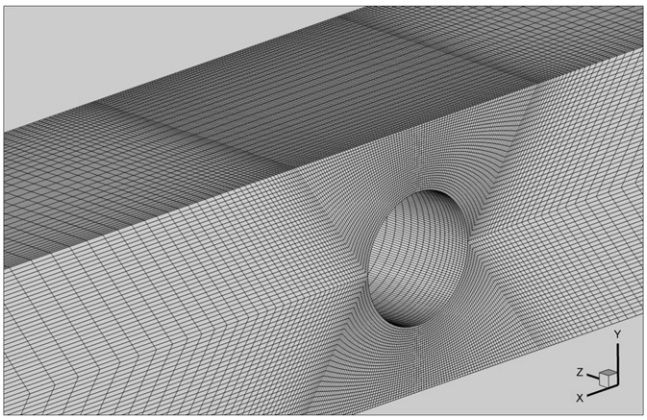

Fig. 4. Zoomed view of the mesh used in the numerical simulations for AR=2.

Table 2
Minimum cell sizes of the computational meshes used.

AR	$(\Delta l/R)_{\min}$	$(\Delta s/R)_{\min}$	$(\Delta r/R)_{\min}$
16	0.050	0.050	0.033
8	0.050	0.050	0.033
2	0.050	0.050	0.033
0.50	0.0125	0.050	0.033

Regarding the boundary conditions, no-slip is assumed at the walls ($\boldsymbol{u}=\mathbf{0}$), while at inlet a uniform velocity field is assumed. Since the inlet channel is long, as in the experiments, the flow becomes fully-developed well upstream of the cylinder. At the outlet, vanishing gradients are assumed for the velocity while pressure is linearly extrapolated from the two upstream cells.

The full computational domain was mapped using block-structured meshes. The inlet and outlet were located 200 and 140 cylinder radii upstream and downstream of the origin of the coordinate system, respectively, to allow complete flow development upstream of the cylinder and to eliminate outlet boundary condition effects in the region of interest. To generate the mesh, the flow domain was divided into 24 blocks and within each block the cells were concentrated near the cylinder region, as illustrated in Fig. 4.

Extensive sets of calculations using meshes with different levels of refinement were carried out by Ferreira (2006) to estimate the numerical uncertainty and select an adequate mesh to provide mesh independent results. The characteristics of the meshes used in this work are presented in Table 2, where $(\Delta l/R)_{\min}$ represents the minimum dimensionless cell size along the cylinder axis, $(\Delta r/R)_{\min}$ the minimum cell size on the radial direction and $(\Delta s/R)_{\min}$ the minimum cell size of the arc length over the cylinder surface.

5. Results and discussion

In addition to the geometric parameters previously defined (AR and BR) the flow characteristics depend also on the Reynolds number (Re), here defined as

$$Re=\frac{\rho UR}{\mu}, \tag{5}$$

where U is the bulk upstream velocity and R is the radius of the cylinder.

The experiments were carried for three aspect ratios, AR=16, 8 and 2 and for each case the results are reported for different planes along the cylinder (constant z/R) and for the symmetry

plane $y/R=0$, as shown in Fig. 2. In the flow visualizations and PIV measurements the Reynolds number was varied between 2 and 40 for $AR=16$ and 8 and between 2 and 70 for $AR=2$, in order to maintain steady flow conditions. For comparison purposes numerical simulations were also carried out for the same steady flow conditions, and additionally the case $AR=0.5$ was also numerically investigated. Additional flow visualizations were also done for unsteady conditions, and compared with numerical predictions.

Both in the experiments and in the numerical simulations under steady flow conditions, the flow was found to be symmetric with respect to planes $y/R=0$ and $z/R=0$.

In Section 5.1 we present the flow visualization results, together with some numerical data, whereas the velocity fields obtained with the PIV technique and additional numerical data are reported in Section 5.2.

5.1. Flow visualizations—flow patterns and recirculation bubble length

Fig. 5 compares the flow visualizations and numerical predictions at the symmetry plane ($z/R=0$) for $AR=16$, 8 and 2, in each case at two values of Re to illustrate the flow pattern within the separated flow region. For all values of AR, the recirculation length, L_v, increases with the increase of Re. A good agreement between the two sets is observed.

For the specific values of $AR=8$ and $Re=29.1$ the spanwise variation of the projected streamlines (i.e., at different values of z/R), is shown in Fig. 6, containing again the corresponding numerical predictions. In this figure the recirculation length, L_v, is also marked at the various cross-section planes and again the comparison between the experimental and numerical data is remarkably good. Qualitatively, the pictures taken for $AR=16$ and $AR=2$, not shown, are similar and the agreement with the numerical results is as good as for $AR=8$, hence no further comparison is shown for conciseness. However, from the whole set of fluid flow visualizations and the corresponding numerical simulations, we were able to construct plots showing the variation of L_v with Re, as explained next.

Fig. 7 shows the spanwise variation of the recirculation length for $AR=16$, 8, 2 and 0.5 as a function of Re. The vortex length is measured at the symmetry plane ($y/R=0$) and the plots show both the experimental (symbols) and numerical (lines) data. At all spanwise locations the recirculation length increases with the Reynolds number (in agreement with the results presented in Fig. 5), and the plots show a non-monotonic variation of L_v/R with z/R, for $AR \geq 2$. There is always a local maximum of L_v at the end wall, followed by an intense reduction in recirculation length with the minimum L_v occurring approximately at a distance of one cylinder radius from the wall for $AR \geq 2$, i.e., at $z/R \approx (AR-1)$. Then, the length of the separated flow region increases again, except for $AR=0.5$. The location of the second maximum depends on AR and Re. For $AR=0.5$, a minimum value of L_v occurs at $z/R=0$ for reasons to be explained below, and this also happens for $AR<0.5$. In any case, for $AR<0.5$ the width of the channel is already smaller than the cylinder radius. For large AR (e.g. $AR=16$ and 8) the minimum L_v near the end wall is followed by an increase to a plateau value, as we move away from this wall, except at the higher Re where the recirculation length reaches a maximum value at about $z/R=11$ for $AR=16$ and at about $z/R=3$ for $AR=8$, before levelling to the plateau value. The differences are small and the detection of this is better seen in the numerical results, shown in Fig. 7a and b. At low AR values, as for $AR=2$, the second maximum of L_v occurs at $z/R=0$ and this peak is actually larger than the peak L_v at the end wall, for the higher values of Re. For $AR=0.5$, the channel span is so small that there is only one maximum of L_v, located at the wall and a local minimum at $z/R=0$. In all cases the experiments show the flow to be symmetric in relation to the $z/R=0$ symmetry plane, therefore the previous discussion also holds for negative values of z/R.

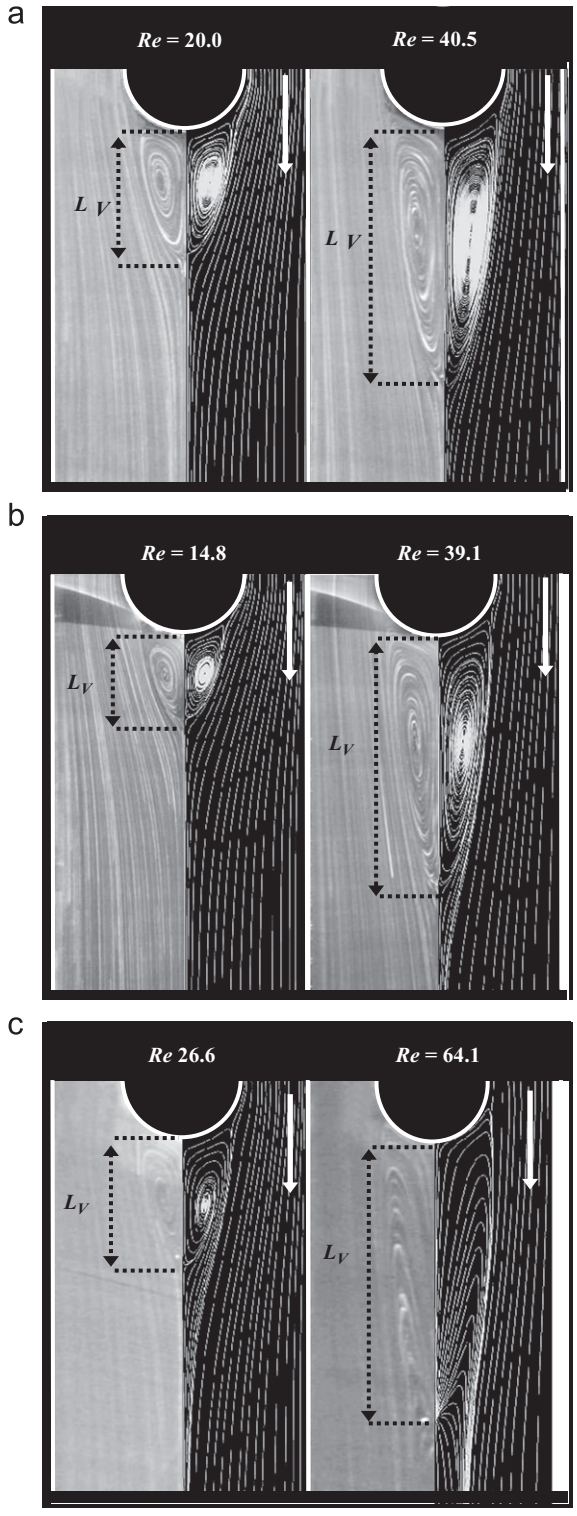

Fig. 5. Experimental (left side) and numerical (right side) streamlines as a function of Reynolds number at the symmetry plane ($z/R=0$) for (a) $AR=16$, (b) $AR=8$ and (c) $AR=2$.

The effect of the Reynolds number on the recirculation length at the $z/R=0$ symmetry plane is shown in Fig. 8a, where it is clear that L_v increases with Re. For $AR=16$, 8 and 2 and for values of

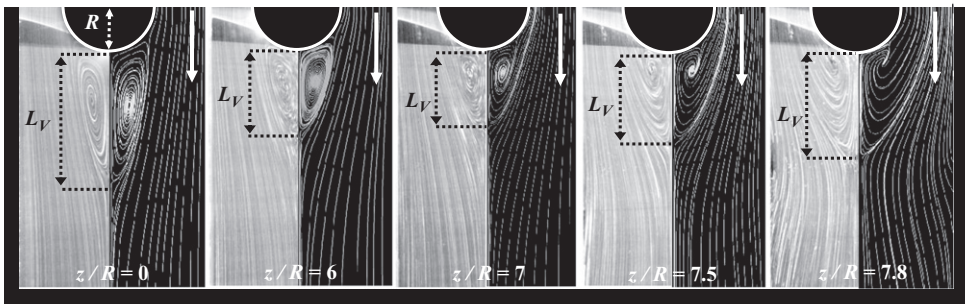

Fig. 6. Experimental (left-hand side) and numerical (right-hand side) projected streamlines for $AR=8$ and $Re=29.1$ as a function of z/R.

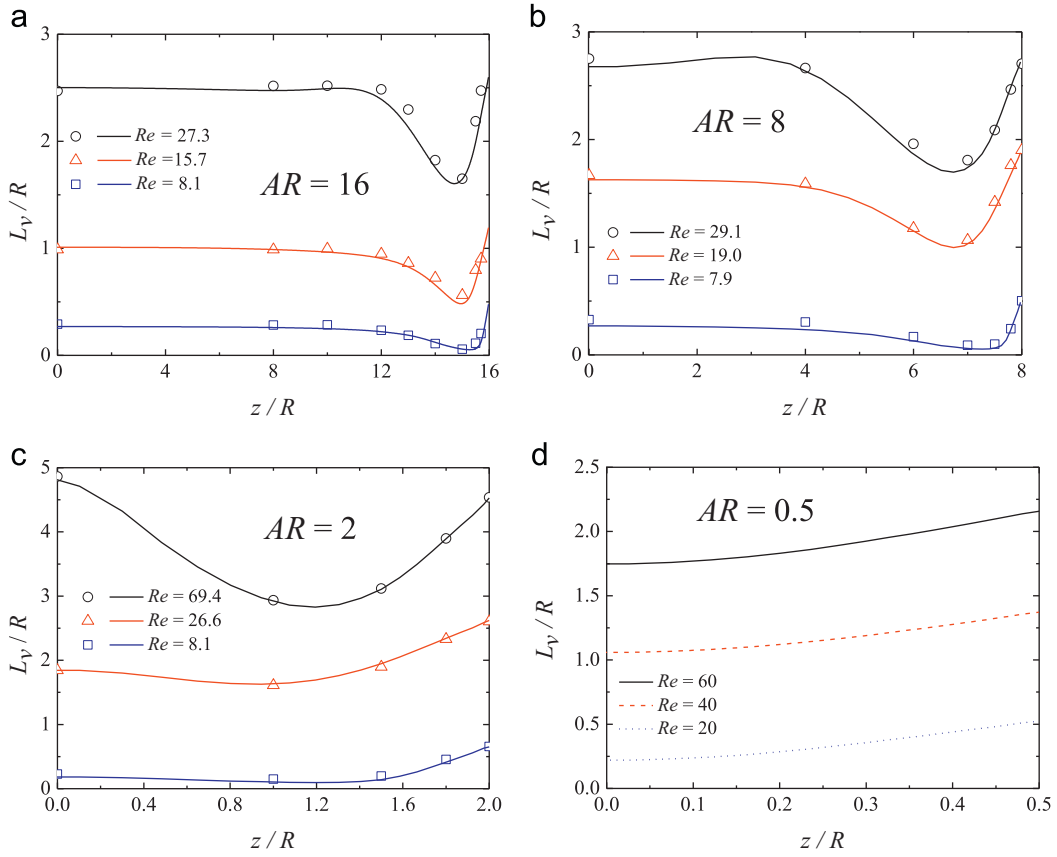

Fig. 7. Spanwise variation of the length of the separated flow region as a function of the Reynolds number at the symmetry plane ($y/R=0$): (a) $AR=16$, (b) $AR=8$, (c) $AR=2$ and (d) $AR=0.5$. Comparison between experiments (symbols) and numerical predictions (lines).

$Re<6$ there is no flow separation. However, for $AR=0.5$ the flow separation appears only for values of $Re\geq 14$, due to the stabilizing effect of the end walls, which approach each other as AR decreases. For large values of AR (e.g. $AR=16$ and 8), the variation of L_v with Re at the $z/R=0$ centreplane is quasi-linear and independent of AR, up to $Re\approx 30$, followed by a decrease in slope, which is stronger for higher values of AR. At $Re\geq 40$ the flow becomes unsteady for $AR=16$ and 8. For $AR=2$ the variation of L_v with Re is quasi-linear up to $Re\approx 45$ and a progressively slower increase of L_v with Re is observed for higher Re. The flow also becomes unsteady for $AR=2$, but for $Re\approx 75$. Thus, as AR decreases there is a clear influence on L_v with smaller values being observed at constant Re and the variation of L_v with Re becoming non-linear at increasingly higher values of Re. The stabilizing effect of the end walls is clearly visible in the numerical results obtained with $AR=0.5$, where now steady flow is observed at least up to $Re=300$ (data for $Re>80$ is not shown in Fig. 8).

Fig. 8b also plots the variation of L_v with Re, but now near the end walls, at the approximate location of the minimum recirculation length, i.e., at $z/R=(AR-1)$. As for the $z/R=0$ symmetry plane, for $AR=16$, 8 and 2 there is no flow separation at $Re\leq 6$ and we observe a linear variation of L_v with Re up to $Re\approx 25$, but with a lower slope than at the symmetry plane. It is also interesting to observe the near collapse of the L_v versus Re curves for the various geometries at the $z/R=(AR-1)$ planes and $Re\leq 25$, in contrast to what is seen at the symmetry plane. This shows that these near end wall flows have essentially the same characteristics and that they are determined by the proximity to the end wall, whereas at the symmetry plane the flow is independent of the end walls for

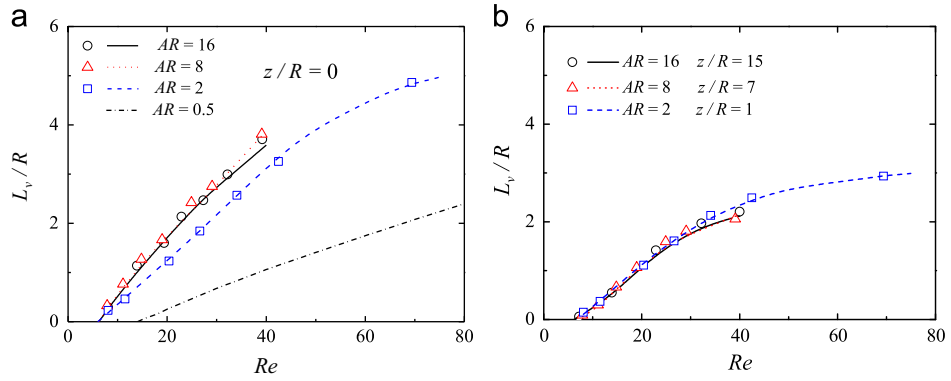

Fig. 8. Variation of the separated flow region length with the Reynolds number: (a) at the symmetry plane ($z/R=0$) and (b) at near end wall planes, $z/R=AR-1$ ($z/R=15$ for $AR=16$, $z/R=7$ for $AR=8$ and $z/R=1$ for $AR=2$). Comparison between experiments (symbols) and numerical predictions (lines).

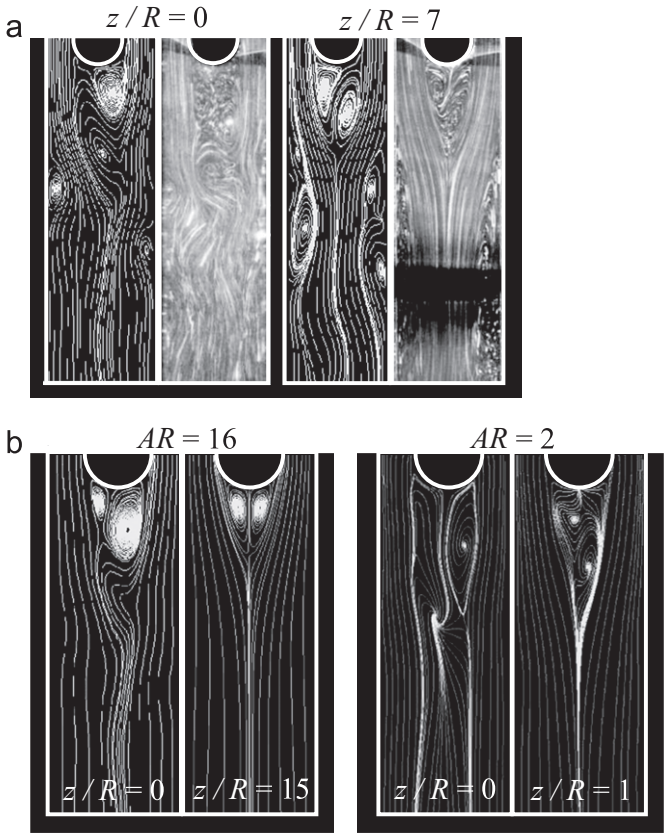

Fig. 9. (a) Experimental pathlines (right-hand side) and numerical predictions of instantaneous projected streamlines (left-hand side) for $AR=8$ and $Re=130.2$ and (b) numerical predictions for $AR=16$ ($Re=45$) and $AR=2$ ($Re=80$).

large values of AR, but starts to be controlled by the end walls as AR decreases below a critical value (of order 1). Note that when $AR \ll 1$ the flow becomes identical to that inside a Hele–Shaw flow cell, where the flow features are precisely controlled by the end wall and flow separation is no longer observed.

At constant z/R planes, Fig. 9a shows instantaneous pathlines obtained from flow visualizations and numerical predictions of instantaneous streamlines for $AR=8$ (projected on the visualization plane), whereas Fig. 9b only shows numerical data for $AR=16$ and 2, taken at the symmetry plane and near the end walls. In all cases the flow patterns are unsteady with Fig. 9a showing a fair agreement between numerical streamlines and experimental pathlines. Note that there was here no attempt to match the instant of time of experiments and predictions within the periodicity cycle. At these Reynolds numbers the free shear layers just started to interact with each other, as a sign of what will happen when the periodic vortex shedding is firmly established. For these Reynolds numbers this interaction only produces a moderate oscillation of the flow patterns on the wake of the cylinder. The same phenomenon can be seen at this stage in the flow around a cylinder with smaller blockage ratio as in the experiments of Coelho and Pinho (2003).

5.2. Velocity field

Fig. 10 shows the influence of Re on the normalized streamwise velocity along the centreline ($y/R=0$ and $z/R=0$) for $AR=16$, 8, 2 and 0.5. These profiles were obtained using both the PIV technique (symbols) and numerical simulation (lines); the agreement between both sets of data is again good. Qualitatively, all velocity profiles are similar upstream of the cylinder and for each value of AR they are essentially independent of the Reynolds number. The upstream influence of the cylinder on the centreline velocity profile is restricted to about four cylinder radii. The value of the normalized velocity at the centreline exceeds 1.5, the centreline normalized velocity for fully-developed flow between two infinite parallel plates, precisely because of the influence of the end walls, which is larger the smaller the value of AR. Indeed, the normalized centreline velocity for fully-developed flow conditions in a rectangular duct is maximum for a square channel ($AR=2$; $u/U=2.096$) and minimum for $AR\to 0$ or $AR\to\infty$ ($u/U=1.5$) as can be easily obtained from the analytical solution for laminar flow in rectangular ducts (White, 1991). Downstream of the cylinder, the influence of the Reynolds number is obviously strong and the recirculation length is seen to increase with the Reynolds number, as previously observed in the flow visualizations. We remind that the end of recirculation corresponds to the location downstream of the cylinder where $u=0$.

Similar normalized profiles of the streamwise velocity are shown in Fig. 11, but now at different spanwise planes, including the centreline for reference. Specifically, the profiles plotted are all at the symmetry plane, $y/R=0$, and comparison is made between the profiles at the centreline ($y/R=0$ and $z/R=0$) and at the line near the end walls where the minimum recirculation length was seen in the flow visualizations, namely at $y/R=0$ and $z/R=(AR-1)$. For all values of AR, the velocity upstream of the cylinder is higher on the centreline than on the line near the end walls as expected and the upstream flow is affected by the presence of the cylinder only in the region $-4\le x/R\le -1$. Along the central region of the geometry the approaching flow decelerates continuously due to the blockage imposed by the cylinder, but in contrast, near the end walls a small flow acceleration is initially observed to occur prior to the deceleration for the geometries with larger aspect ratio ($AR=16$ and 8). This suggests

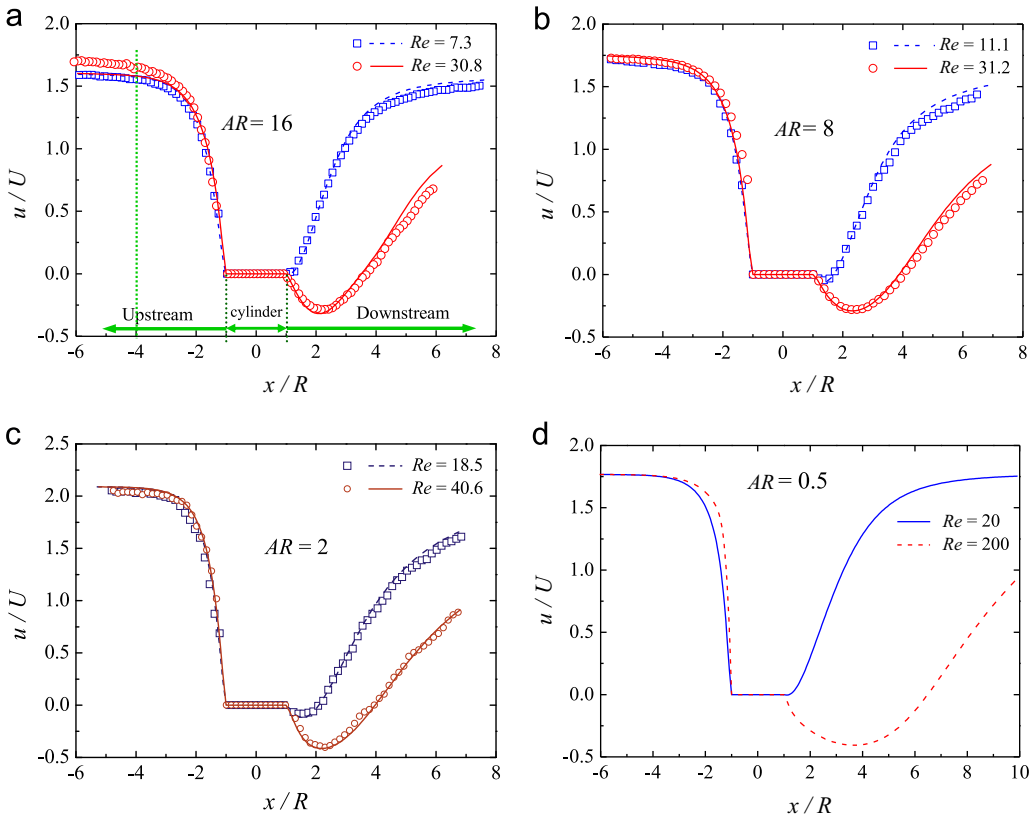

Fig. 10. Streamwise velocity profile along the centreline ($y/R=0$, $z/R=0$) for two values of Re: (a) $AR=16$, (b) $AR=8$, (c) $AR=2$ and (d) $AR=0.5$. Comparison between experiments (symbols) and numerical predictions (lines).

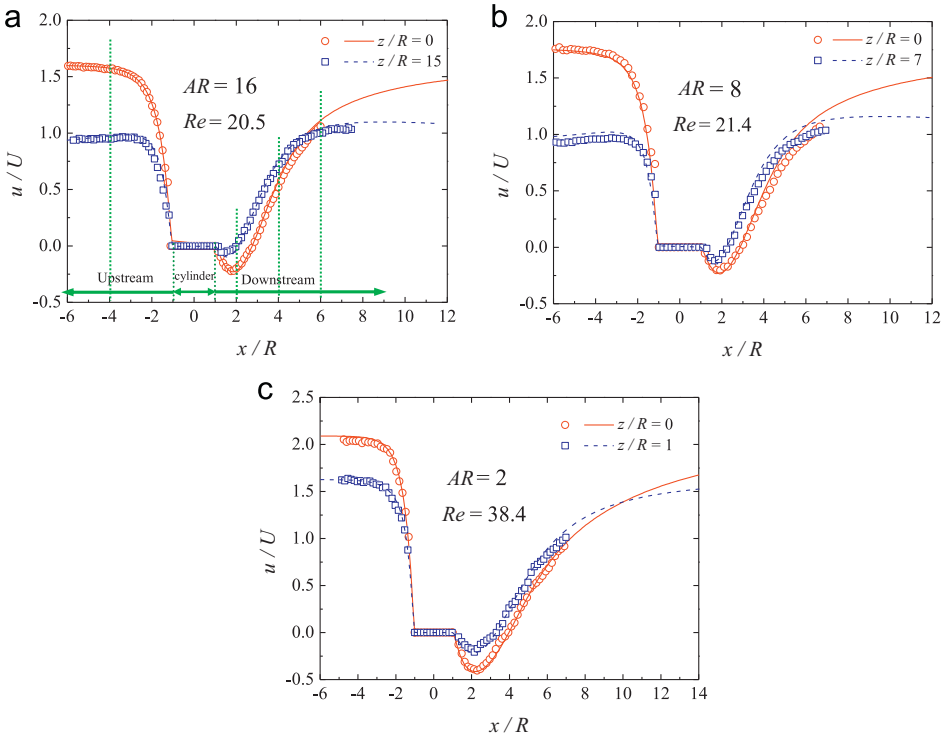

Fig. 11. Streamwise variation of streamwise velocity for $y/R=0$. Comparison between the profiles on the centreline ($z/R=0$) and near the end walls ($z/R=AR-1$): (a) $AR=16$, $Re=20.5$; (b) $AR=8$, $Re=21.4$; and (c) $AR=2$, $Re=38.4$. Comparison between experiments (symbols) and numerical predictions (lines).

the local appearance of a small spanwise velocity component towards the end wall and that there is a fundamental difference between the flow characteristics at high and low *AR*.

Downstream of the cylinder, and for all *AR*, flow recovery starts earlier in the near-wall plane than on the centreline, because of the shorter recirculation length (cf. Fig. 7), leading to higher

velocities there and in spite of the retarding effect of the end walls. Further downstream, however, the ever present retarding effect of the end walls takes over and the near-wall velocities stabilize to lower values than at the symmetry plane as already observed far upstream under fully developed flow conditions. At the higher Reynolds numbers the cross-over of the two velocity profiles take place at increasingly longer distances from the rear stagnation point.

In order to understand the flow characteristics and in particular the effect of the end walls, we present in Figs. 12–14 transverse profiles of the normalized velocity at the symmetry ($z/R=0$) and near end wall planes ($z/R=AR-1$) at one upstream and three downstream locations. Figs. 12, 13 and 14 pertain to $AR=16$, 8 and 2, respectively, the Reynolds number is approximately the same ($Re\approx 26$) and for each case the upstream location is $x/R=-4$ and the downstream profiles are at $x/R=2$, 4 and 6. These locations are also marked in Fig. 11a. Since all flows are symmetric only half the profiles are shown. The figures contain experimental data obtained by PIV (symbols) and the corresponding numerical data (lines) and the agreement is good. In all cases, and as shown in Figs. 12a, 13a and 14a, the upstream profiles at $x/R=$-4 approach the analytical solution (lines) for fully-developed laminar flow in a rectangular duct (White, 1991), especially for the smaller *AR*, since the influence of the cylinder is negligible for $x/R<$ -4, and so the velocities are always higher on the symmetry plane than on the near end wall plane.

The downstream profiles (Fig. 12b–d, 13b–d and 14b–d) are in agreement with the previous observations that the recirculation length is shorter near the end walls and consequently the flow there develops faster. Thus, at $x/R=2$ (Figs. 12b, 13b and 14b) the velocities are higher near the end walls than at the symmetry plane region from $y/R=0$ to a location that varies with *AR* ($|y/R|\approx 0.9$ for $AR=16$ and $|y/R|\approx 1$ for $AR=8$; for $AR=2$ the numerical simulations indicate a value of $|y/R|<0.7$, whereas for the experiments the difference between the two profiles are within experimental uncertainty). This non-monotonic variation of the cross-over point is related to the change of type of the flow: for small *AR* the flow characteristics are everywhere determined by the end walls, whereas for large *AR* the flow in the central region of the domain is essentially independent of the end wall effects and depends primarily on the Reynolds number. In the gap between the cylinder and the side walls (at $|y/R|=2$) the velocities will be higher in the symmetry plane region than near the end walls as a consequence of the larger approach flow velocities, cf. Figs. 12a, 13a and 14a. However, these differences are not proportional to the corresponding upstream flow velocities, and the actual velocity difference between both velocity profiles in the gap is smaller than in the approach flow (for all values of *AR* the velocity profiles in Figs. 12b, 13b and 14b are not too different), on account of a secondary flow developing along the cylinder, in the spanwise direction, which brings fluid from the central region to the near end wall region. It is this secondary flow that induces the velocity peaks in the *y*-direction, which are strongly enhanced by the increasing flow inertia. Indeed the loci of the velocity peaks are also dependent on the Reynolds number.

Moving further downstream to $x/R=4$ (cf. Figs. 12c, 13c and 14c for $AR=16$, 8 and 2, respectively) and then to $x/R=6$ (Figs. 12d, 13d and 14d) a similar behaviour to that found at $x/R=2$ is also observed, but with the cross-over point at a different location with lower peak velocities and located closer to the $y/R=0$ symmetry plane as expected. At $x/R=6$ there are no longer cross-over points for the $AR=2$ case since the separated flow regions end earlier and the flow redevelopment process is consequently in a more advanced stage than at larger *AR*.

Spanwise profiles of normalized streamwise velocity at the symmetry plane $y/R=0$ and at the downstream location $x/R=4$ are shown in Fig. 15 for different values of *Re*. The shape of these

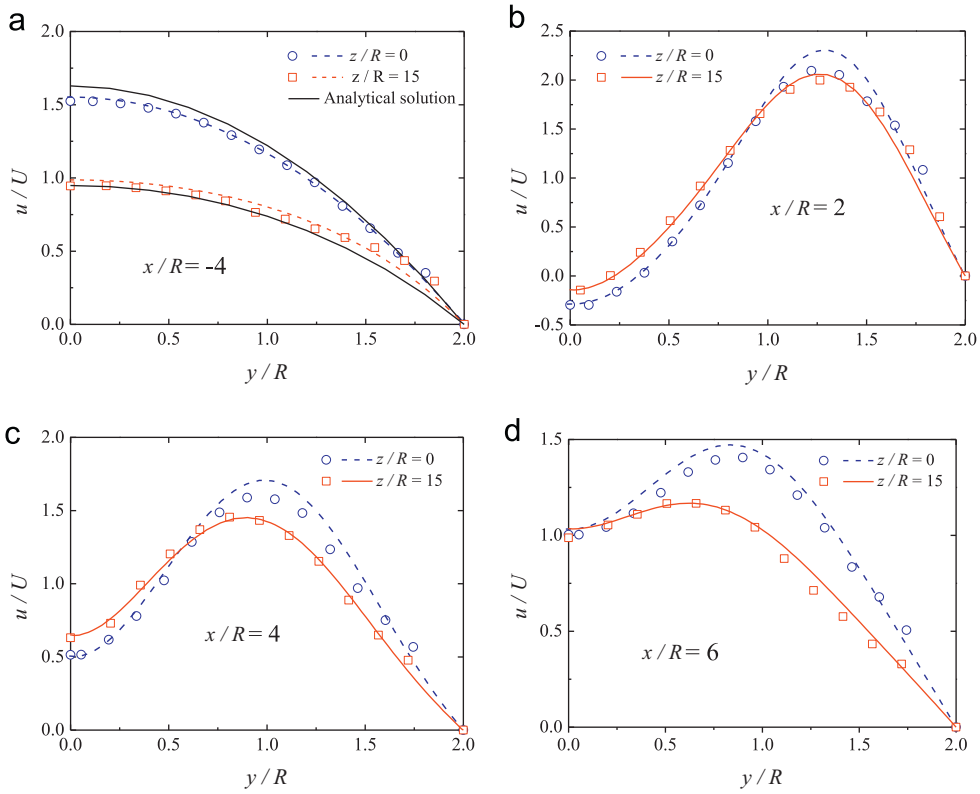

Fig. 12. Transverse variation of streamwise velocity at the symmetry plane ($z/R=0$) and near the end wall ($z/R=15$) for $AR=16$ and $Re=25.3$: (a) $x/R=-4$, (b) $x/R=2$, (c) $x/R=4$, and (d) $x/R=6$. Comparison between experiments (symbols) and numerical predictions (lines).

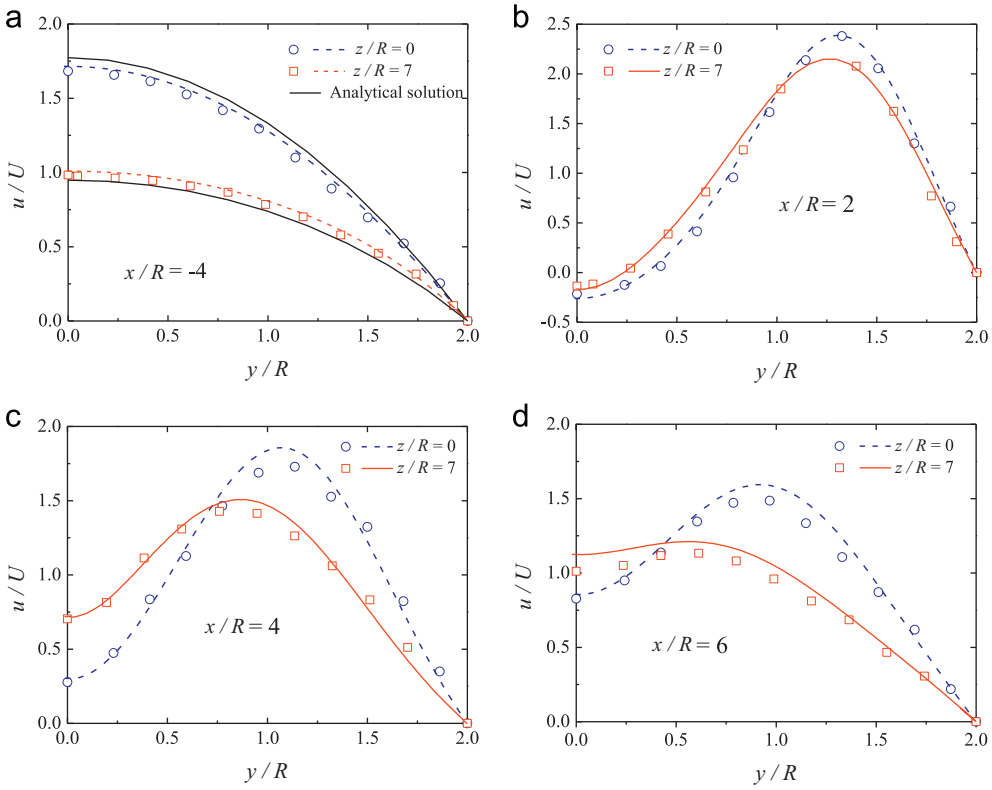

Fig. 13. Transverse variation of streamwise velocity at the symmetry plane ($z/R=0$) and near the end wall ($z/R=7$) for $AR=8$ and $Re=25.6$: (a) $x/R=-4$, (b) $x/R=2$, (c) $x/R=4$, and (d) $x/R=6$. Comparison between experiments (symbols) and numerical predictions (lines).

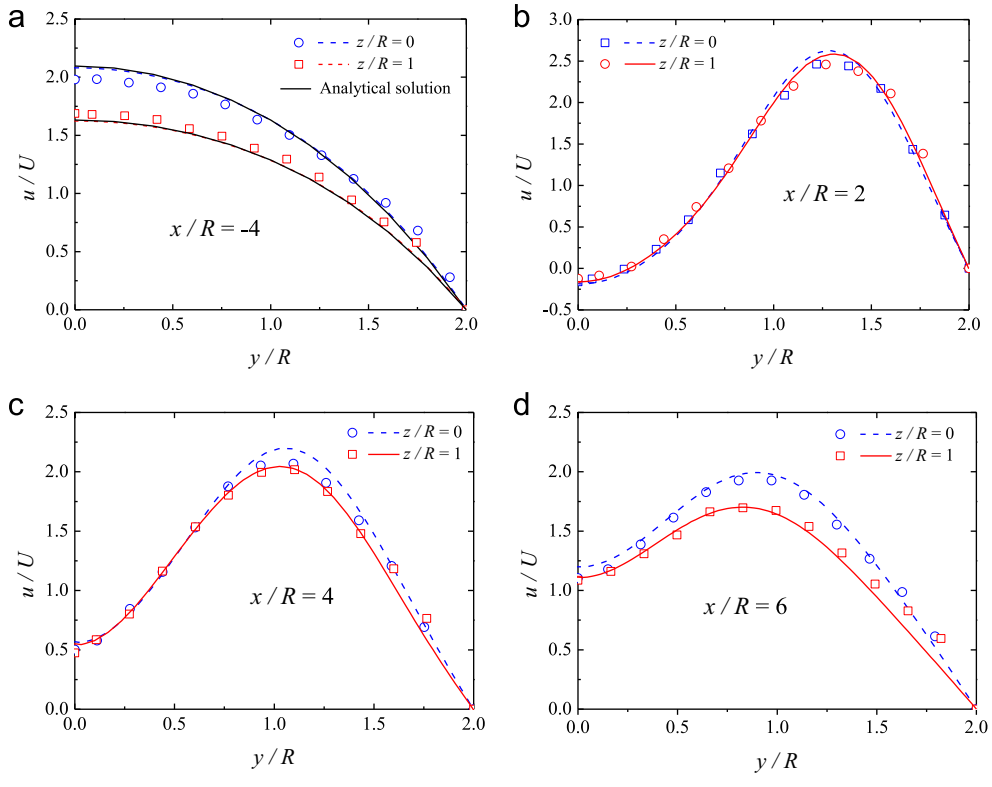

Fig. 14. Transverse variation of streamwise velocity at the symmetry plane ($z/R=0$) and near the end wall ($z/R=1$) for $AR=2$ and $Re=26.1$: (a) $x/R=-4$, (b) $x/R=2$, (c) $x/R=4$, and (d) $x/R=6$. Comparison between experiments (symbols) and numerical predictions (lines).

profiles is inverse to those of the corresponding profiles of recirculation length shown in Fig. 7, i.e., where there is a local maximum in recirculation length, a local velocity minimum is observed and vice versa. These results confirm the existence of velocity peaks near the end walls, which are enhanced by flow inertia. The curves corresponding to cases with a large separated

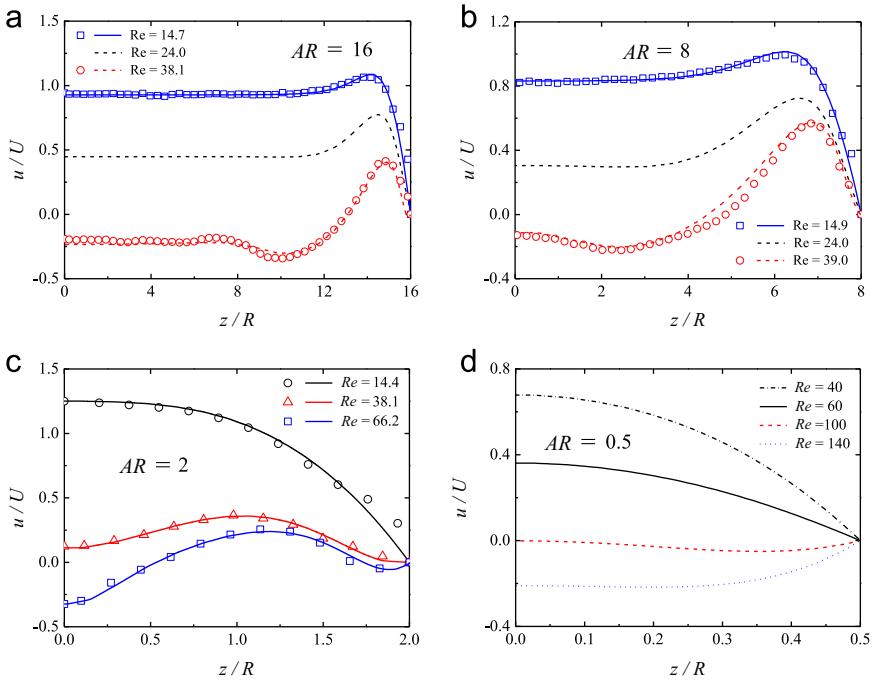

Fig. 15. Spanwise variation of the normalized streamwise velocity downstream of the cylinder ($x/R=4$) and on the symmetry plane $y/R=0$ as a function of the Reynolds number: (a) $AR=16$, (b) $AR=8$, (c) $AR=2$ and (d) $AR=0.5$. Comparison between experiments (symbols) and numerical predictions (lines).

flow region (higher *Re*), Figs. 15a and b, show that next to the strong positive velocity peak there is a region of minimum velocity. This local velocity deficit is possibly due to fluid that feeds into the nearby near-wall jet.

The difference in the behaviours at $AR=16$, 8 and 2, even at the high Reynolds number flow, is a consequence of the qualitative differences imposed by the end walls upon the flow at the core of the duct. The downstream profiles at the lower Reynolds number ($Re\approx 15$) develop fast especially for lower *AR*. For $AR=16$ and 8 the influence of the end walls is confined to a region near those walls and does not propagate to the centre of the duct, where the flow is essentially controlled by the vicinity of the side walls of the duct, parallel to the cylinder axis. In contrast, for $AR=2$ the end walls are as important as the side walls and affect significantly the flow at the symmetry plane, $z/R=0$, because even though its region of influence may be of similar physical size it corresponds to a proportionally larger volume of the flow domain than at larger values of *AR*.

5.3. Numerical results and mechanism for the velocity peaks

Considering that the comparison between experimental and numerical data of Figs. 5–15 showed a good agreement, in what follows only numerical data are used to explore in detail the flow dynamics and help interpret the causes for the velocity peaks. The main issues that we aim to address with this study are to determine the value of *AR* below which the effects of the end walls dominate the whole flow and what are the causes of the appearance of the velocity peaks in its various forms.

According to the results shown in Sections 5.1 and 5.2 the velocity peaks are located at $z/R\approx(AR-1)$. For higher *AR* this location is near the end walls and far away from the centreplane (i.e. $z/R\gg 0$), while for lower *AR* this location is in the centreplane (i.e. $z/R=0$) and the velocity profiles show a parabolic shape. The velocity peaks near the end walls tend to disappear for $AR\lesssim 6$, when the influence of the end walls becomes as important as the influence of the side walls.

Velocity peaks are not exclusive of high Reynolds number flows and have been reported at low *Re* flow conditions with viscoelastic fluids by Verhelst and Nieuwstadt (2004) (cf. their Fig. 31 at a Deborah number of 2.72). Interestingly, in Figs. 16a and b we show, based on numerical simulations, that velocity peaks are also observed in the spanwise profiles of streamwise velocity at $y/R=0$ and downstream locations (e.g. at $x/R=4$), even under creeping flow conditions (i.e. in the limit $Re\to 0$) for Newtonian fluids. These profiles pertain to aspect ratios of 2, 8, 16, 32 and 128 and clearly illustrate the existence of local velocity peaks near the end walls at $Re=0$ and increasing as *AR* is raised. Note that in these creeping flow cases there is no flow separation. The shapes of the velocity profiles and of the velocity peaks at $Re=0$ in Fig. 16 are different from those at the large Reynolds number flows with separation in Fig. 15, but not too different from the shape of the profile at $Re\approx 15$ in the same Fig. 15 despite the existence of flow separation. Creeping flow is simulated numerically deleting the convective term in the momentum equation. The transient term is retained since a time marching algorithm is used. When steady flow is achieved the transient term cancels out, and the Stokes equations are solved corresponding exactly to creeping flow conditions.

The behaviour of the flow around a confined cylinder and in particular the causes for the appearance of the velocity peaks in its various forms are discussed next. It is appropriate to start with a limiting case, such as creeping flow ($Re\approx 0$), which is dominated by viscous forces that generate the pressure contours shown in Fig. 17a. At large aspect ratios and upstream of the cylinder, the fluid will have to accelerate to circumvent the obstacle, with the corresponding pressure reduction being higher near the end-wall than in the centre. Hence a negative spanwise pressure gradient (in the coordinate system used) appears and the upstream fluid acquires a spanwise velocity from the centre to the end wall region as is shown in the contour plots of Fig. 17c and in the corresponding contours of streamwise velocity of Fig. 17b. This effect starts to be observed at about four cylinder diameters upstream of the obstacle and by pushing fluid towards the near-

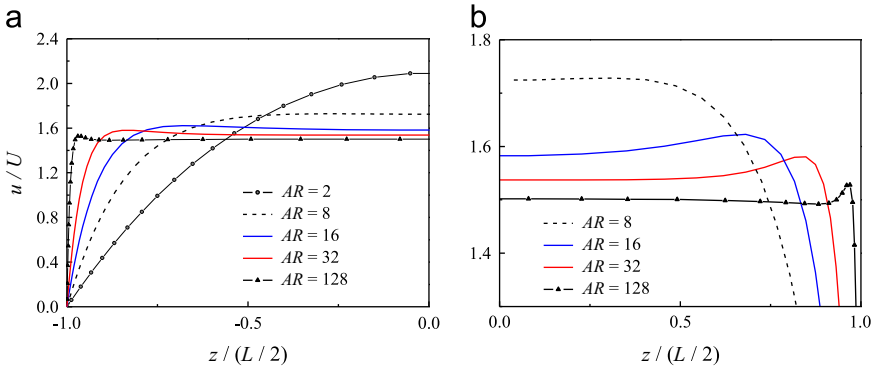

Fig. 16. Axial velocity profiles at $y/R=0$ and $x/R=4$ as a function of spanwise coordinate for various aspect ratios and $Re=0$. A smaller range of u/U is shown in part (b) in order to better illustrate the existence of small velocity overshoots under creeping flow conditions for large values of *AR*. Only numerical results are shown.

wall region, the upstream region with a peak velocity shown in Figs. 16 and 17b is formed.

In spite of the locally increased flow near the end-wall, the pressure decrease of the flow around the cylinder is less here than in the centre, so that the flow downstream of the cylinder has now a higher pressure near the end-wall than in the centre (cf. Fig. 17a) thus creating a positive spanwise pressure gradient that moves the fluid from the near-wall region into the centre. This is seen both as contours of negative spanwise velocity in Fig. 17c as well as in the symmetric orientation of contours of streamwise velocity in Fig. 17b. This fore-aft symmetry of the velocity field is precisely a major characteristic of creeping flows of purely viscous fluids around symmetric obstacles. Also note that the $\Delta z/L$ distance of the peaks to the end wall increases in inverse proportion to *AR*, but this corresponds to the same distance $\Delta z/R$.

This picture is only changed by inertia, which reduces the time available for τ_{xz} to act and for this reason the peak velocity at $Re \approx 15$ in Fig. 15a is found closer to the end wall than the peak at $Re=0$ in Fig. 16, for the same value of *AR*. Needless to say further downstream of $x/R \approx 4$ this diffusive flux continues to act and the velocity peaks will be smoothed out and the velocity profile becomes that of the fully-developed rectangular duct flow.

Under creeping flow conditions, as *AR* decreases, the τ_{xz} stresses increase and this smoothes the localized peaks and the velocity profiles acquire the parabolic shape typical of the Hele–Shaw flow, where the flow is now totally dominated by the large gradients of τ_{xz}. Inertia counteracts this effect and this is well shown in Fig. 15c (or in Fig. 7c for the corresponding profiles of L_v), where we see the velocity peak moving away from the centreline at $Re=15$ to $z/R>1$ as the Reynolds number further increases. Therefore, as the *Re* increases the flow is perturbed by inertial effects, which become superimposed and eventually dominate the above diffusion mechanism.

For large aspect ratios, such as $AR=16$, we have essentially the flow picture explained above, except that the increase in the Reynolds number leads to the formation of a separated flow region all along the cylinder span, whose length is affected by the proximity of the end wall, since the strong streamwise adverse pressure gradient downstream of the cylinder also varies in the spanwise direction. Consequently, a region of minimum recirculation length appears at the same location of the velocity peaks, where the adverse pressure gradient is weaker, and this is especially noticeable for flows with strong separation (cf. Fig. 7a). At large *Re* the flow in the region of small L_v is able to negotiate the cylinder with minimum pressure loss, i.e., it separates later and consequently is able to recover pressure more efficiently than fluid farther from the wall, as is confirmed in Fig. 18 which shows a later flow separation and a shorter recirculation near the end wall. There are two main causes for this behaviour. The slowdown imposed by the wall to the fluid as it approaches the cylinder is not very strong, but it is sufficient to reduce locally the *Re* and this leads to a smaller recirculation length very much as the effect of *Re* on L_v depicted in Fig. 8. Additionally, there is a secondary flow in the spanwise direction that appears within the separated flow helping the fluid in the region of minimum L_v to better sustain the local adverse pressure gradient. Note that this fluid came from the upstream region along the end-wall as depicted in Fig. 19. This fluid, which had been pushed toward the cylinder edges upstream of the obstacle, flows now towards the centre on the downstream side of the cylinder.

The better pressure recovery in the region of minimum L_v leads to a higher pressure there than further away from the wall, where pressure recovery is poorer. Additionally a spanwise pressure gradient is seen to exist behind the cylinder, which is consistent with the spiralling secondary flow inside the open separated flow region from the end walls to the symmetry plane, a mechanism enhanced by flow inertia and illustrated in Fig. 19. This secondary flow takes fluid out of the minimum L_v near end wall region and into the symmetry plane region, while simultaneously fluid must enter the separated flow region at the near wall region. These near end wall features are also confirmed in the spiralling stream traces on the right-half of Fig. 18. In contrast, upstream of the cylinder a spanwise pressure variation is also seen to exist (cf. Fig. 20) but now with lower pressures near the end wall and higher pressure in the centre, which is consistent with the slight deviation of the upstream streamlines from the centre toward the end-wall observed in Fig. 19 that seems to constitute the feeding mechanism of the secondary flow. At large *Re* these inertial boundary layer mechanisms far outweigh the acceleration mechanism described earlier and the velocity peaks acquire their special sharp forms. Reducing aspect ratio brings into action the discussed smoothing effect of the shear stress τ_{xz}.

A final observation is needed in regard to the increase in L_v at the end wall itself. The boundary layer arguments invoked above for the near wall region, that a low velocity fluid is able to negotiate better the cylinder and recover pressure more efficiently are only valid if the region is not being constantly drained of momentum by viscous forces as happens at the end wall. At this location flow energy is being drained by viscosity simultaneously at the cylinder wall and at the end-wall hindering the capability of the fluid to negotiate the cylinder in spite of the lower local Reynolds number, so the outcome is an early flow separation and a sharp increase in L_v.

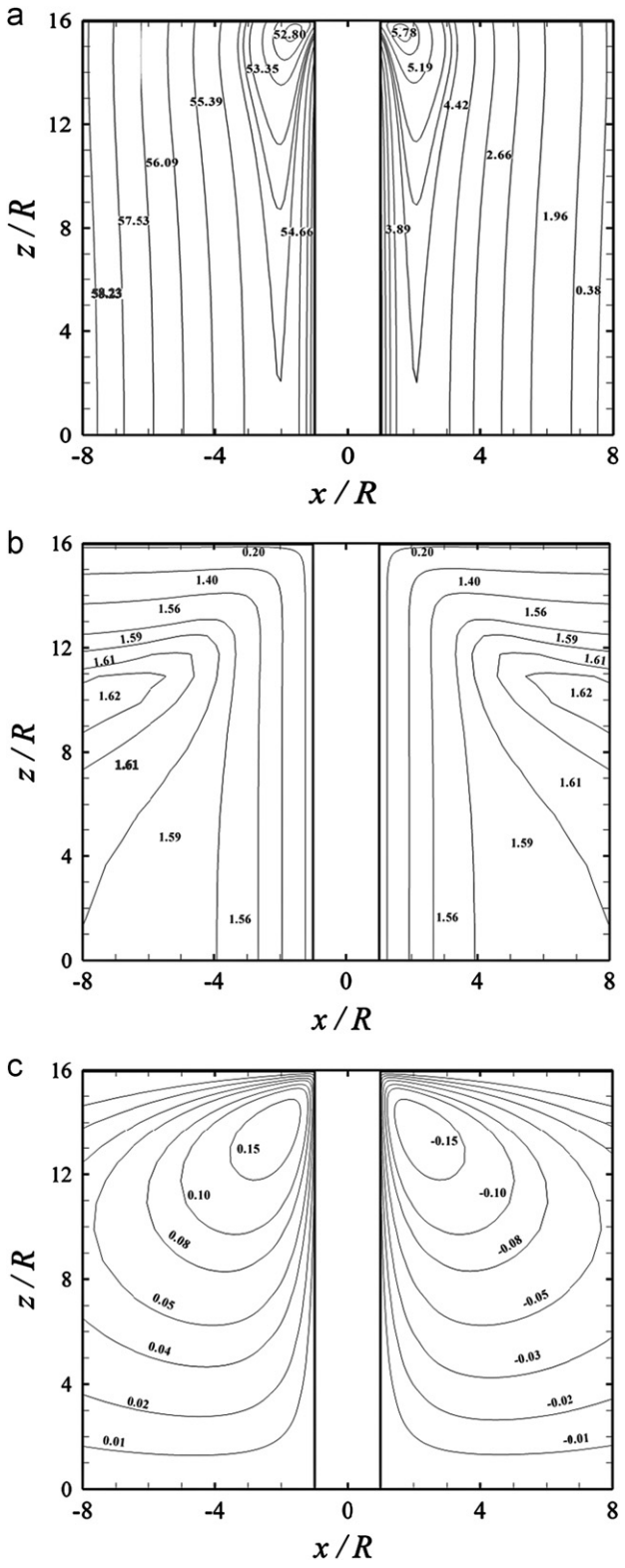

Fig. 17. Contours of normalized pressure and velocity predicted numerically at $y/R=0$ for $AR=16$ and $Re=0$: (a) pressure, $(p-p_{ref})/(\mu U/R)$; (b) streamwise velocity, u/U; and (c) spanwise velocity, w/U.

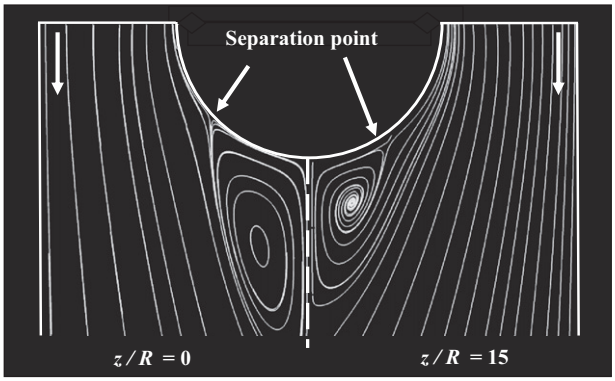

Fig. 18. Numerical predictions for $AR=16$ and $Re=20$ to illustrate the location of the separation point for $z/R=0$ and $z/R=15$ (projected streamlines).

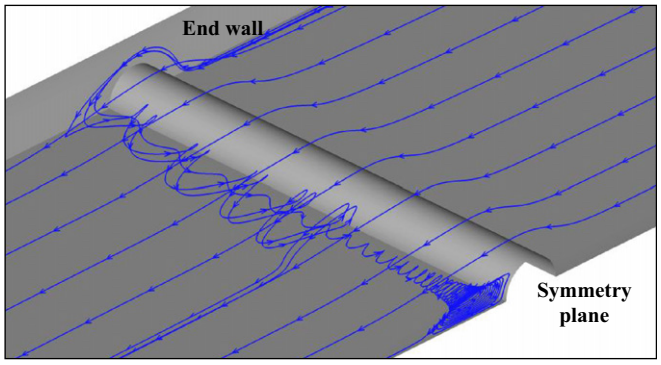

Fig. 19. Illustration of some particle pathlines predicted numerically near the cylinder for $AR=16$ and $Re=39.2$.

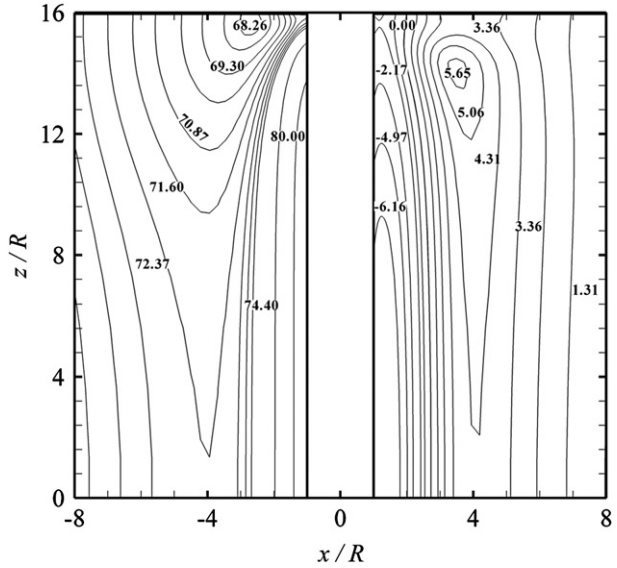

Fig. 20. Contours of normalized pressure, $(p-p_{ref})/(\mu U/R)$, predicted numerically at centreplane $y/R=0$ for $AR=16$ and $Re=20$.

6. Conclusions

An experimental and numerical investigation was carried out on the laminar steady flow around a confined cylinder placed in a rectangular duct with a 50% blockage ratio duct to assess the effects of the channel aspect ratio. The aspect ratio of the duct varied between $AR=0.5$ and $AR=32$ (in the experiments $AR=2$, 8 and 16 were considered) and the Reynolds number varied between creeping flow conditions ($Re\rightarrow 0$) up to the onset of time-dependent flow. The experiments relied on flow visualizations, using streak photography, and detailed velocity measurements by PIV, both taken in various planes around the cylinder.

The numerical calculations were carried out with a finite volume numerical method and the predictions compare very well with the experimental results. The good agreement between numerical and experimental results indicated that a more detailed study could be carried out numerically to explore flow conditions not studied experimentally and to help to interpret the results. Both the experimental and numerical results always showed symmetry with respect to planes $y/R=0$ and $z/R=0$ under the steady flow conditions investigated.

For all values of *AR*, the upstream influence of the cylinder occurs up to $x/R \approx -4$. Downstream of the cylinder the velocity fields have an inverse shape to the corresponding profiles of recirculation length, i.e., where there is a local minimum in recirculation length (near the end walls), we find a local velocity maximum and vice versa. The results showed that the recirculation length increases with *Re* regardless of the *AR*, and also varies along the neutral *z*-direction. A maximum recirculation length is observed at the end walls and for high *AR* a local minimum recirculation length is found near these end walls at about one cylinder radius distance, i.e., at $z/R \approx (AR-1)$. This local minimum in L_v coincides with the location of a maximum value of streamwise velocity. The fluid in this region is able to sustain better the adverse streamwise pressure gradient than on the centreplane, as shown by a later separation angle and consequently it is able to recover more pressure as it flows around the cylinder. At large values of *AR* the separated flow region is open, i.e., there is also a spiralling spanwise secondary flow inside the separated flow region, from the end wall towards the symmetry plane.

At very low *Re* there is no longer flow separation and the maximum velocity peaks are all due to the excessive braking role of the end wall, which forces a local fluid acceleration for mass conservation which the very small diffusive spanwise–streamwise momentum flux (τ_{xz}) is unable to smooth out. These peaks disappear when the aspect ratio is reduced (for $AR < 6$) and by implication the τ_{xz} stress increases strongly. Then, the influence of the end walls becomes as important as that of the side walls, and as the flow tends to that of a Hele–Shaw apparatus ($AR \to 0$) the velocity variations become parabolic and the end walls dominate the flow. However, inertia counteracts the role of this diffusive momentum flux even at small values of *AR* so much that at $AR=2$ and $Re=38$ there are still velocity peaks. This emphasizes the importance of inertial effects in this flow.

Acknowledgements

The authors acknowledge the financial support provided by Fundação para a Ciência e a Tecnologia (FCT), COMPETE and FEDER through projects PTDC/EME-MFE/114322/2009, REEQ/928/EME/2005 and REEQ/298/EME/2005. V.M. Ribeiro would also like to thank FCT for financial support through scholarship SFRH/BD/44737/2008.

References

Adrian, R.J., 2005. Twenty years of particle image velocimetry. Exp. Fluids 39, 159–169.
Alves, M.A., Oliveira, P.J., Pinho, F.T., 2003. A convergent and universally bounded interpolation scheme for the treatment of advection. Int. J. Numer. Methods Fluids 41, 47–75.
Brown, R.A., Mckinley, G.H., 1994. Report on the VIIIth international workshop on numerical-methods in viscoelastic flows. J. Non-Newton. Fluids 52, 407–413.
Cantwell, B., Coles, D., 1983. An experimental-study of entrainment and transport in the turbulent near wake of a circular-cylinder. J. Fluid Mech. 136, 321–374.
Chakraborty, J., Verma, N., Chhabra, R.P., 2004. Wall effects in flow past a circular cylinder in a plane channel: a numerical study. Chem. Eng. Process. 43, 1529–1537.
Coelho, P.M., Pinho, F.T., 2003. Vortex shedding in cylinder flow of shear-thinning fluids I. Identification and demarcation of flow regimes. J. Non-Newton. Fluids 110, 143–176.
Dealy, J., Plazek, D., 2009. Time–temperature superposition – a users guide. Rheol. Bull. 18, 16–31.
Escudier, M.P., Gouldson, I.W., Oliveira, P.J., Pinho, F.T., 2000. Effects of inner cylinder rotation on laminar flow of a Newtonian fluid through an eccentric annulus. Int. J. Heat Fluid Flow 21, 92–103.
Ferreira, H.H., 2006. Escoamento de fluidos newtonianos e viscoelásticos em torno de um cilindro: estudo numérico de efeitos tridimensionais. Master's thesis (in Portuguese) Faculdade de Engenharia da Universidade do Porto, Porto.
Gerich, D., Eckelmann, H., 1982. Influence of end plates and free ends on the shedding frequency of circular-cylinders. J. Fluid Mech. 122, 109–121.
Gerrard, J.H., 1966. Mechanics of the formation region of vortices behind bluff bodies.
J. Fluid Mech. 25, 401–413.
Hiemenz, K., 1911. Die Grenzschicht an einem in dem gleichförmigen Flüssigkeitsstrom eingetauchten geraden Kreiszylinder. University of Göttingen, Germany.
Kawaguti, M., 1953. Numerical solution of the Navier–Stokes equations for the flow around a circular cylinder at Reynolds number-40. J. Phys. Soci. Jpn. 8, 747–757.
Lee, T., Budwig, R., 1991. A study of the effect of aspect ratio on vortex shedding behind circular cylinders. Phys. Fluids, 3.
Leweke, T., Williamson, C.H.K., 1998. Three-dimensional instabilities in wake transition. Eur. J. Mech. B—Fluids 17, 571–586.
Nieuwstadt, F., Keller, H.B., 1973. Viscous flow past circular cylinders. Comput. Fluids 1, 59–71.
Nishimura, T., 1986. Flow across tube banks. In: Cheremisinoff, P. (Ed.), Encyclopedia of Fluid Mechanics. Gulf Publishing Company, pp. 763–785.
Nishioka, M., Sato, H., 1974. Measurements of velocity distributions in the wake of a circular-cylinder at low Reynolds-numbers. J. Fluid Mech. 65, 97–112.
Norberg, C., 1994. An experimental investigation of the flow around a circular-cylinder—influence of aspect ratio. J. Fluid Mech. 258, 287–316.
Oliveira, M.S.N., Alves, M.A., Pinho, F.T., McKinley, G.H., 2007. Viscous flow through microfabricated hyperbolic contractions. Exp. Fluids 43, 437–451.
Oliveira, M.S.N., Alves, M.A., Pinho, F.T., McKinley, G.H., 2008a. Newtonian fluid flow through microfabricated hyperbolic contractions. Exp. Fluids 3, 437–457.
Oliveira, M.S.N., Rodd, L.E., McKinley, G.H., Alves, M.A., 2008b. Simulations of extensional flow in microrheometric devices. Microfluid. Nanofluid. 5, 809–826.
Oliveira, P.J., Pinho, F.T., Pinto, G.A., 1998. Numerical simulation of non-linear elastic flows with a general collocated finite-volume method. J. Non-Newton. Fluids 79, 1–43.
Payne, R.B., 1958. Calculations of unsteady viscous flow past a circular cylinder. J. Fluid Mech. 4, 81–86.
Rao, M.K., Sahu, A.K., Chhabra, R.P., 2011. Effect of confinement on power-law fluid flow past a circular cylinder. Polym. Eng. Sci. 51, 2044–2065.
Sahin, M., Owens, R.G., 2004. A numerical investigation of wall effects up to high blockage ratios on two-dimensional flow past a confined circular cylinder. Phys. Fluids 16, 1305–1320.
Sen, S., Mittal, S., Biswas, G., 2009. Steady separated flow past a circular cylinder at low Reynolds numbers. J. Fluid Mech. 620, 89–119.
Sheely, M.L., 1932. Glycerol viscosity tables. Ind. Eng. Chem. 24, 1060–1064.
Strouhal, V., 1878. Ueber eine besondere Art der Tonerregung. Ann. Phys. 241, 216–251.
Sumer, B.M., Fredsoe, J., 1997. Hydrodynamics around cylindrical structures. Adv Ser Coastal Eng, Vol. 12.
Telionis, D.P., Gundappa, M., Diller, T.E., 1992. On the organization of flow and heat-transfer in the near wake of a circular-cylinder in steady and pulsed flow. J. Fluid Eng.—Trans. ASME 114, 348–355.
Thom, A., 1933. The flow past circular cylinders at low speeds. In: Proceedings of the Royal Society of London Series A—Containing Papers of a Mathematical and Physical Character, vol. 141, pp. 651–669.
Thompson, M., Hourigan, K., Sheridan, J., 1996. Three-dimensional instabilities in the wake of a circular cylinder. Exp. Therm. Fluid Sci. 122, 190–196.
Verhelst, J.M., Nieuwstadt, E.M., 2004. Visco-elastic flow past circular cylinders mounted in a channel: experimental measurements of velocity and drag. J. Non-Newton. Fluids 116, 301–328.
von Kármán, T., 1911. Über den Mechanismus des Widerstandes, den ein bewegter Körper in einer Flüssigkeit erfärt. Göttinger Nachrichten mathematisch-physikalische Klasse, 509–517.
White, F.M., 1991. Viscous Fluid Flow. McGraw-Hll.
Williamson, C.H.K., 1996a. Three-dimensional wake transition. J. Fluid Mech. 328, 345–407.
Williamson, C.H.K., 1996b. Vortex dynamics in the cylinder wake. Annu. Rev. Fluid Mech. 28, 477–539.
Zdravkovich, M.M., 1997. Flow Around Circular Cylinders: Fundamentals, vol.1. Oxford University Press, New York.
Zdravkovich, M.M., 2003. Flow Around Circular Cylinders: Applications, vol. 2. Oxford University Press, New York.